JGR Atmospheres

RESEARCH ARTICLE
10.1029/2024JD042349

Impact of the East Asian Stratospheric Intrusion on Lower Tropospheric Ozone in the Yangtze River Delta

Jinpeng Lu[1,2], Xin Huang[1,2,3], Xueyu Zhou[1,2], Lijie Yang[1,2], Sijia Lou[1,2,3], Zilin Wang[1,2,3], Jiawei Xu[1,2], and Aijun Ding[1,2,3]

[1]School of Atmospheric Sciences, Nanjing University, Nanjing, China, [2]Collaborative Innovation Center for Climate Change, Nanjing, China, [3]Frontiers Science Center for Critical Earth Material Cycling, Nanjing University, Nanjing, China

Key Points:

- Sustained ozone pollution in the Yangtze River Delta in May 2023 was partly attributed to stratospheric ozone-rich air
- Stratospheric intrusion is driven by westerly jets and downwelling behind the trough accompanying the low-pressure system at 46°–60°N
- WRF-Chem simulation confirms near-surface ozone increases ~12 ppb in the Yangtze River Delta due to stratospheric intrusion

Supporting Information:

Supporting Information may be found in the online version of this article.

Correspondence to:

X. Huang,
xinhuang@nju.edu.cn

Citation:

Lu, J., Huang, X., Zhou, X., Yang, L., Lou, S., Wang, Z., et al. (2025). Impact of the east Asian stratospheric intrusion on lower tropospheric ozone in the Yangtze River Delta. *Journal of Geophysical Research: Atmospheres*, *130*, e2024JD042349. https://doi.org/10.1029/2024JD042349

Received 29 AUG 2024
Accepted 22 JUN 2025

Author Contributions:

Conceptualization: Sijia Lou, Aijun Ding
Formal analysis: Jinpeng Lu, Lijie Yang, Sijia Lou, Aijun Ding
Funding acquisition: Sijia Lou, Aijun Ding
Investigation: Jinpeng Lu, Xueyu Zhou, Lijie Yang, Sijia Lou, Jiawei Xu, Aijun Ding
Methodology: Jinpeng Lu
Validation: Zilin Wang
Visualization: Jinpeng Lu
Writing – original draft: Jinpeng Lu
Writing – review & editing: Jinpeng Lu, Zilin Wang

Abstract Tropospheric ozone (O_3) pollution has aroused increasing attention in past decades, especially in China, with escalating near-surface O_3 levels. Apart from photochemical reactions, stratospheric intrusion (SI) also contributes to tropospheric O_3 pollution. In this study, a strong SI event that greatly influenced the near-surface O_3 pollution was identified in May 2023. To quantitatively analyze the contribution to surface O_3 over the Yangtze River Delta (YRD), meteorological reanalysis data, in situ observations, and a regional meteorology-chemistry coupled model were integrated. Our findings reveal that the severe O_3 pollution observed over the YRD region cannot be solely attributed to photochemical processes. Noteworthily, a distinct signal of stratospheric air masses injecting into the troposphere was observed, indicating a more complex interplay between atmospheric chemical and physical processes. The clustering analysis of the backward trajectories shows that the O_3-rich air masses injected into the lower troposphere are primarily driven by westerly jets and downwelling behind the troughs accompanying the low-pressure weather system at 46°N–60°N. The stratospheric O_3-rich air masses can be transported to the YRD region driven by the strong downwelling occurring with a high-altitude wind field toward the south. Using the regional meteorology-chemistry model Weather Research and Forecasting model coupled with Chemistry (WRF-Chem) with real-time input of the upper chemical boundary conditions, it is estimated that such regionally transported SI O_3 contributed more than 12 ppb to surface O_3 pollution over the YRD region.

Plain Language Summary Tropospheric ozone (O_3) is detrimental to human health and ecosystem productivity. As its primary natural source, stratospheric intrusion (SI) has been recognized as one contributor to tropospheric O_3. Focusing on an O_3 pollution event on 7–12 May 2023, when SI occurred at 46°–60°N in East Asia, O_3-rich air masses from the stratosphere injected into the lower troposphere, resulting in more severe O_3 pollution even in urban areas.

1. Introduction

Tropospheric ozone (O_3) is an important pollutant (Young et al., 2018), although it contributes only about 10% of the total O_3 in the atmosphere. Due to its strong oxidative capacity, tropospheric O_3 has adverse effects on air quality, crop yields, human health, and ecosystems (Cooper, 2019; Gaudel et al., 2018), and has wide-ranging implications for atmospheric chemistry and climate change (Lefohn et al., 2018; Wang et al., 2024). Tropospheric O_3 is the key precursor of the hydroxyl radicals, which mainly contributes to the removal of many chemically reactive gases (Wang et al., 2017). It is the third most important greenhouse gas, after carbon dioxide (CO_2) and methane (CH_4), and is responsible for global warming (Gaudel et al., 2018). Therefore, an understanding of the spatial and temporal distribution of tropospheric O_3 and its influencing factors is extremely important and has attracted increasing attention globally (Ding, Fu, et al., 2013; Monks et al., 2015; Xue et al., 2021).

From a global perspective, tropospheric O_3 originates from two sources: photochemical production within the troposphere and dynamical injection from the stratosphere. Tropospheric O_3 is formed by sunlight-driven photochemical reactions involving biogenic emitted volatile organic compounds (VOCs), nitrogen oxides ($NO_x = NO + NO_2$), and other pollutants (CH_4, carbon monoxide (CO)) (Chameides et al., 1992; Li et al., 2024; Sillman, 1995; Wang et al., 2020a, 2024; Xia et al., 2022; Xu et al., 2021). The photochemical production mainly occurs in areas with dense anthropogenic emissions, for example, the Beijing–Tianjin–Hebei region, Yangtze River Delta (YRD) region, and Pearl River Delta (Lu, Zhang, Chen, et al., 2019). The O_3 concentrations are regulated by meteorological conditions, precursor emissions, photolysis rate, and deposition. The relationship

between O_3 and its precursors exhibits a non-linear pattern that varies across different regions (Assareh et al., 2016; Li et al., 2021; Lin et al., 2015). Dry deposition is a major process (Clifton & Patton, 2021) of O_3 removal from the atmosphere in addition to nocturnal NO_2-titration (Tang et al., 2012). Meteorological conditions play an important role in O_3 pollution, not only through transport but also by affecting natural emissions and chemical rates, adding complexity to mitigation efforts (Li et al., 2020; Lu, Zhang, Zhao, et al., 2019).

Besides photochemical production within the troposphere, stratospheric O_3 can also be transported to the troposphere by stratospheric intrusion (SI) processes (Ding & Wang, 2006). In order to effectively control near-surface O_3 pollution, it is necessary to effectively control local pollutant emissions and to strengthen joint control of surrounding sources. Furthermore, the impact of the SI processes on near-surface O_3 also needs to be considered (Langford et al., 2012; Lin et al., 2012; Xia et al., 2023). Since the thermal, dynamical, and chemical characteristics of the stratosphere are different from those of the troposphere, SI processes can transport stratospheric O_3-rich air masses directly into the troposphere under certain atmospheric circulation conditions (Holton et al., 1995) and contribute to near-surface O_3 and subsequent pollution (Wang, Wang, et al., 2020). The SI could be characterized by O_3-rich air, anomalously high potential vorticity (PV), and low water vapor. Tropopause fold is a key mechanism of SI, associated with the downward transport of stratospheric air to the troposphere (Stohl et al., 2003; Yang et al., 2022). The dynamic processes leading to SI include tropopause folds in the vicinity of the polar and subtropical jets (Akritidis et al., 2010; Gerasopoulos et al., 2006), Brewer–Dobson circulation (Salby & Callaghan, 2006), cut-off lows (Ancellet et al., 1994; Price & Vaughan, 1993), blocking high pressure, breaking gravity waves (Krasauskas et al., 2021; Lamarque et al., 1996), the Rossby Wave Breaking (Wang et al., 2023), and mesoscale convective complexes (Poulida et al., 1996), etc. (Ganguly & Tzanis, 2011; Li et al., 2015). The SI plays an important role in determining the tropospheric O_3 budget in the mid-high latitudes (Langford et al., 2012; Tarasick et al., 2019) that is estimated to account for only 5%–10% of the tropospheric O_3 (Stevenson et al., 2006), and contributes 16% to the variation in O_3 in the mid-latitude mid-troposphere of the Northern Hemisphere (Olsen et al., 2019). Consequently, SI is also a significant contributor to the changes of tropospheric O_3 (Hong et al., 2024) and near-surface O_3 (Langford et al., 2018; Lefohn et al., 2014).

Eastern China, as one of the most densely-populated and rapidly-developing regions in the world, has been suffering from O_3 pollution in the past decades (Ding, Fu, et al., 2013). Severe O_3 pollution episodes have been reported frequently in eastern China and aroused concerns from both the government and the public, especially in the YRD region (Ding et al., 2008; Huang et al., 2021; Xu et al., 2008). In China, most studies on SI events have focused on the Qinghai-Tibet Plateau and the northeast of China (Chen et al., 2014; Zhao et al., 2019) while SI events in the YRD region are less investigated. Although the highest O_3 concentration often occurs from May to July in the YRD region (Wang et al., 2017), the O_3 pollution in the YRD region includes the photochemical production and also the contribution of the SI process. Nanjing, a megacity located in the YRD region, also faced extreme O_3 pollution events. Several studies have employed the Model for Ozone and Related Chemical Tracers in the Stratosphere and Mesosphere (MOZART) to quantify the contribution of a SI to surface O_3 in Nanjing with a magnitude of about 10 ppb in summertime (Wang, Wang, et al., 2020).

In this study, we focus on the possible processes of O_3 pollution sources in the YRD region. In Section 2, the data sets and models used in this study as well as the methods, are described. The results are structured as follows. In Section 3, we show the observational evidence of SI and its impacts on surface O_3 pollution. Meanwhile, we analyze the weather process and transport pathway of SI O_3 and quantify regional impacts over the YRD region with the WRF-Chem model. This study ends with a discussion and a conclusion of the main findings in Section 4.

2. Data and Methods

2.1. Observational Data

2.1.1. Air Quality and Meteorological Observation

Available ground observations in China are used in this study. Since 2013, real-time air quality monitoring at more than 1,500 stations has been openly available from the air monitoring data center of the Ministry of Ecology and Environment of the People's Republic of China. This air quality monitoring network with an hourly temporal resolution covers most parts of China and provides more information on the spatial distribution and its evolution characteristics across China (Huang et al., 2018). The six prescribed basic categories of air pollutants are sulfur

dioxide (SO_2), nitrogen dioxide (NO_2), CO, O_3, and particulate matter ($PM_{2.5}$ and PM_{10}). In particular, the SO_2, NO_2, CO, and O_3 concentrations are the concentrations in the reference state (atmospheric temperature of 298.15 K and atmospheric pressure of 1013.25 hPa), and the $PM_{2.5}$ and PM_{10} concentrations are the concentrations in the live state (actual atmospheric temperature and pressure at monitoring time). In this study, O_3, NO_2, and CO were applied to analyze the evolution of O_3 during the SI events. The ground dew point temperature (T_d) and other meteorological parameters are available with observational data from an automatic meteorological station archived in the National Oceanic and Atmospheric Administration (NOAA) National Climatic Data Center (NCDC).

2.1.2. Radiosonde Measurements

The present study utilizes radiosonde data with a temporal resolution of 12 hr, which can be obtained from the website of the University of Wyoming (Gui et al., 2017; Sun et al., 2023). It contains the sounding data obtained from all over the world twice or four times daily. This data set provides twice daily (00:00 and 12:00 UTC) atmospheric soundings. Their radiosonde profile comprises various meteorological profiles, including geopotential height, water vapor pressure, temperature, T_d, relative humidity (RH), etc., at certain pressure levels (Linsha et al., 2024; Sun et al., 2023). In this study, T_d and RH over 300–1,000 hPa were used to analyze the air mass characteristics.

2.2. Meteorological Reanalysis Data

The fifth generation of European Center for Medium-Range Weather Forecasts (ECMWF) atmospheric reanalysis (ERA5) as the newest generation of reanalysis data is used in SI analysis in this study (Hersbach et al., 2020; Zhang et al., 2022). The fine temporal resolution of 1 hr and a spatial resolution of 0.25° × 0.25° (Bartusek et al., 2023) of the ERA5 data set enable a detailed analysis of the evolution of weather systems. There are 37 levels in the vertical direction from 1,000 hPa to 1 hPa. We collected the variables of O_3, vertical velocity (ω), u-component of wind (U), v-component of wind (V), geopotential height (Z), and potential vorticity (PV) to diagnose SI occurrences. The ERA5 O_3 product is a comprehensive data set generated through global numerical modeling combined with multi-source observational data assimilation. The ozone simulations in ERA5 are primarily driven by the Integrated Forecasting System (IFS), which dynamically simulates ozone formation, transport, and depletion processes across the troposphere and stratosphere, accounting for photochemical reactions, meteorological interactions, and boundary layer dynamics. The ERA5 O_3 assimilates different satellite observations, including Microwave Limb Sounder (MLS) and Ozone Monitoring Instrument (OMI), and shows good agreement with the In-service Aircraft for a Global Observing System (IAGOS) profiles and the Atmospheric Infrared Sounder (AIRS) satellite O_3 in the upper troposphere and lower stratosphere (Wang, Wang, et al., 2020). Despite some limitations of ERA5 reanalysis data (https://climatedataguide.ucar.edu/climate-data/era5-atmospheric-reanalysis), the study focuses on the variable characteristics of tropospheric ozone. Moreover, the YRD region is predominantly a plain region and the impact of topography on the vertical direction is relatively small, so it is reasonable to use ERA5 data to verify the impact of SI O_3 events on lower tropospheric O_3 (Ou-Yang et al., 2022; Wang, Wang, et al., 2020).

2.3. Regional Meteorology-Chemistry Coupled Simulation

The Weather Research and Forecasting (WRF) model used in this study is a fully compressible non-hydrostatic mesoscale numerical forecasting model developed by the National Center for Atmospheric Research (NCAR) and the National Center for Environment Prediction (NCEP). The Weather Research and Forecasting model coupled with Chemistry (WRF-Chem) includes a dynamical and a chemical module, which integrates various gas phase chemistry and meteorology-chemistry-aerosol-radiation-cloud interactions via direct, semi-direct, and indirect effects (Grell et al., 2005; Xu et al., 2021). The version 3.7 of WRF-Chem was performed to simulate the impact of SI on near-surface O_3 over the YRD region. The simulation domain is centered at 35.0°N, 110.0°E, with a grid spacing of 20 km. Inside the model, biogenic emissions are generated by the Model of Emissions of Gases and Aerosols from Nature (MEGAN). NCEP global final analysis data (FNL) was used as the initial and lateral boundary conditions of meteorological variables with a 1° × 1° spatial resolution that was updated every 6 hr.

Since the WRF-Chem model itself does not yet take into account stratospheric chemistry, this study couples the real-time input of upper chemical boundary conditions to compensate for the lack of stratospheric O_3 chemistry in the WRF-Chem model. The real-time upper boundary condition (UBC) originates from the Whole Atmosphere Community Climate Model (WACCM), which is updated every 6 hr. By coupling the concentrations of various chemical species (e.g., O_3, NO, NO_2, HNO_3, CH_4, CO, N_2O, and N_2O_5) from the top of the troposphere to the upper boundary obtained from the real-time simulation output of the WACCM to be consistent with the real-time concentrations. Two groups of simulations are performed in this study: the no UBC simulations (NOUBC) and UBC simulations (UBC). The simulations were conducted over the period 6–14 May 2023. For all the simulation runs, the first 6 days of integration were considered as model spin-up. Therefore, the differences between the UBC and the NOUBC (labeled as UBC–NOUBC) are used for identifying the impacts of the SI on the YRD region.

2.4. Source Identification Calculation and Cluster Analysis

Stratospheric O_3 intrusion can affect O_3 concentrations in the intrusion region, and also affect surrounding regions through regional transport processes (Lu, Zhang, Zhao, et al., 2019). We used the Lagrangian particle dispersion modeling (LPDM) to analyze the impacts of regional transport processes on YRD O_3. The LPDM model has been widely applied in atmospheric environment studies for its advantages of stability and traceability (Ding, Wang, & Fu, 2013; Huang et al., 2016; Wang, Huang, et al., 2020). Based on the Hybrid Single-Particle Lagrangian Integrated Trajectory (Hysplit), the model was widely applied to simulate mass diffusion, trajectory, and deposition (Stein et al., 2015). Based on 3D gridded real-time meteorological data (Global Data Assimilation System, GDAS), LPDM can simulate the trajectory of an air mass arriving at any location. GDAS's strength lies in real-time assimilation of multi-source observations (e.g., satellites, radiosondes, and ground stations), ensuring high accuracy and timeliness of meteorological variables (e.g., wind, temperature, humidity). It is widely used in pollution source attribution, meteorological research, and emergency response. After some particles were released at a given point, the Euler method was used for the calculation of the concentration portion, and the Lagrangian method was used for the calculation of the advection and diffusion of the particles. LPDM calculates the positions of the particles in the forward or backward transport at the release height over time by averaging wind and turbulent transport. In this study, the model was run for 72 hr backward with particles released at an altitude of 1,500 m (where the wind field is more stable and pollutants are more easily transported over long distances) above Nanjing at 12:00 LT on 9 May to estimate the influence of SI on the surface O_3. The residence time of particles was used to identify the "footprint" retroplume.

After analyzing the backward trajectories, the Trajstat software in the model can be used to cluster them based on spatial similarity. Cluster analysis enables the trajectories of the backward flows over a period to be categorized and summarized. In this study, cluster analysis was used to analyze the composition of the incoming air masses at the target point and the percentage of trajectories.

3. Results

3.1. Observational Evidence of SI and Its Impacts on Surface O_3 Pollution

Severe O_3 pollution often hits the YRD region from May to July, which has been attributed to the photochemical reactions from anthropogenic emissions and SI process (Huang et al., 2021; Wang, Wang, et al., 2020). On 7–12 May 2023, the YRD region experienced a continuous extreme O_3 pollution. Figure 1a shows the time series of observational O_3 and NO_2 concentrations in Nanjing, a typical densely-populated city in YRD, recorded by air quality monitoring stations. A high near-surface O_3 pollution event occurred in Nanjing during this period. Since the night of 6 May, the observational O_3 concentration has increased significantly, and the O_3 concentration exceeded 83 ppb during the daytime on 9 May, reaching nearly 120 ppb (Figure 1a). Although the O_3 concentration was slightly lower on 10 May, the O_3 concentration remained high level for several days thereafter (Figure 1a). During the corresponding period, the NO_2 concentration remained at a low level and then gradually increased (Figure 1a). In addition to Nanjing, other YRD cities such as Shanghai and Hangzhou showed the same observational O_3 and NO_2 characteristics during the same time period (Figure S1 in Supporting Information S1). Compared with the climatology during 2013–2022, there was a positive O_3 anomaly and a negative NO_2 anomaly starting from 6 May over Nanjing, Shanghai and Hangzhou (Figures S2a–S2c in Supporting Information S1). Moreover, the CO has also been a negative anomaly on 7–12

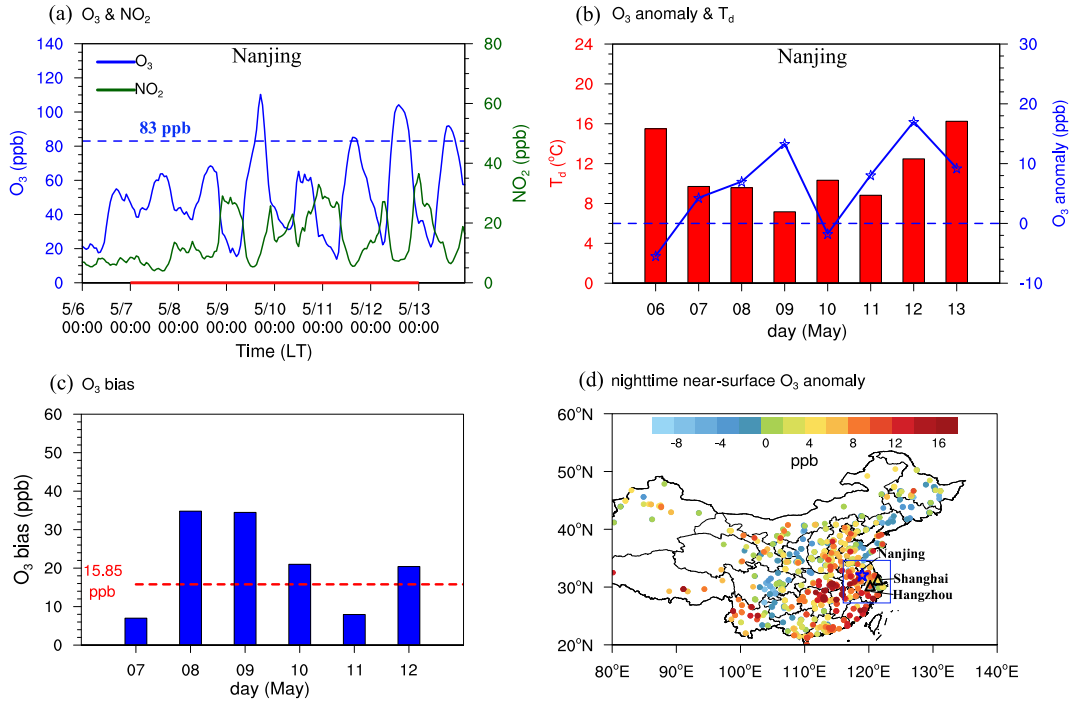

Figure 1. (a) Time series of observational O_3 (solid blue line) and NO_2 (solid green line) concentrations, (b) daily O_3 anomaly (blue line) and T_d (red bar) over Nanjing on 6–13 May 2023. (c) O_3 bias between NOUBC simulation and observation, (d) spatial distribution of nighttime (20:00 LT–06:00 LT) observational near-surface averaged O_3 anomalies on 7–12 May 2023. The observational data are recorded by air quality monitoring stations. In panel (a), the dashed blue line shows the reference value of O_3 (83 ppb), the red line on the *X*-axis indicates the time period affected by stratospheric ozone intrusion. In panel (c), the dashed red line shows the reference value of the monthly averaged O_3 bias in May (15.85 ppb) derived from the NOUBC simulation. In both (b, d), the anomalies in 2023 are obtained by subtracting the average for the same period of 2013–2023 (the same as follows). The blue pentagram symbol in panel (d) indicates the location of Nanjing (the same as follows), and the boxed area represents the YRD region.

May (Figures S2d–S2f in Supporting Information S1). It suggests that the O_3 photochemical production has declined compared with the climatology in the YRD region. For the more inland western YRD area, which is generally downwind from the entire YRD under prevailing winds between northeast and southeast. Therefore, the regional characteristics of pollutants in west YRD cities such as Nanjing are inherently important for the assessment of the regional impacts of the YRD pollution. Therefore, we next analyze the O_3 pollution event in the YRD region mainly focusing on Nanjing. The daily averaged T_d on 7 May decreased rapidly compared with 6 May and remained at a low value until 12 May, then returning to the 6 May's level on 13 May (Figure 1b) over Nanjing. Meanwhile, positive O_3 anomalies began on 7 May, and near-surface O_3 had been increasing with decreasing T_d in Nanjing (Figure 1b).

By using the meteorology-chemistry coupled WRF-Chem model, which only includes tropospheric chemical processes, it is indicated that the simulated near-surface O_3 was much lower than the observed O_3 over Nanjing during this pollution episode (~52.4 ppb). Quantitatively, the O_3 model bias during this event was higher than the monthly averaged bias (15.85 ppb) in May (Figure 1c). Figure 1d shows the spatial distribution of nighttime (20:00 LT–06:00 LT) observational near-surface averaged O_3 anomalies during 7–12 May. It was found that the nighttime near-surface O_3 over the YRD region was a positive anomaly on 7–12 May (Figure 1d). Given the diminishing photochemical process at night and a high-level nighttime O_3 since 7 May (Figure 1a), and the vertical direction in most areas in the YRD region is a downwelling motion when the wind is northeast at 850 hPa (Figure S3 in Supporting Information S1). There are relatively weak near-surface O_3 chemical production processes (Figure S4 in Supporting Information S1) and O_3 from higher altitude continuously affecting the of Nanjing since 7 May (Figures S4 and S5 in Supporting Information S1); therefore, the near-surface O_3 pollution over the YRD region may be subject to non-photochemical processes like SI O_3.

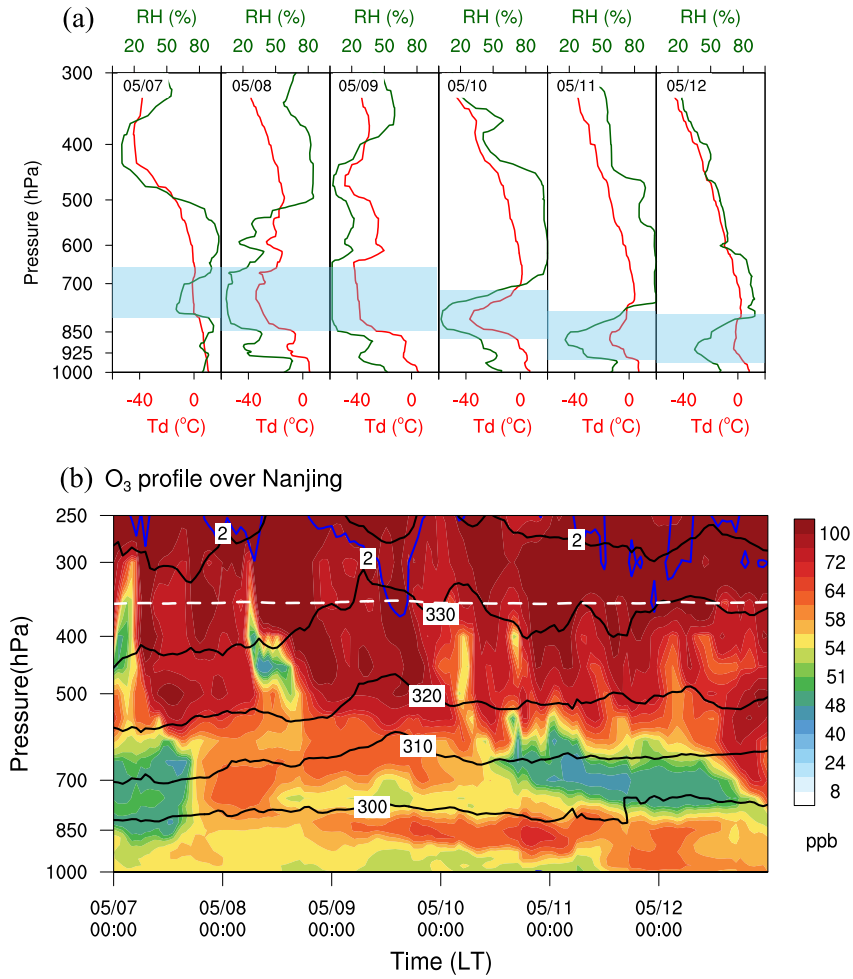

Figure 2. (a) Vertical RH and T_d profiles (08:00 LT) over Nanjing on 7–12 May 2023 based on radiosonde data. (b) Temporal evolution of the vertical distribution of O_3 over Nanjing on 7–12 May 2023 from ERA5 data. White dashed line indicates the height of the thermal tropopause, blue solid line represent the PV values of 2PVU ($1PVU = 10^{-6}\ K \cdot m^2 \cdot s^{-1} \cdot kg^{-1}$), black solid line indicates the potential temperature, and the contour interval is 10 K.

To investigate the impact of SI on Nanjing, we analyzed vertical RH and T_d profiles (08:00 LT) over Nanjing on 7–12 May based on sounding observation and found that the RH and T_d started to reduce below 700 hPa on 7 May (local time) (Figure 2a), which showed that Nanjing was getting affected by dry and cold air masses. However, dry and cold air masses at 400 hPa could not contribute to near-surface ozone on 7 May (Figure 2a). The dry-cold air masses descended to 700–850 hPa at 08:00 LT on 8 May and gradually went down to lower altitudes in the following days (Figure 2a). It is well known that stratospheric air is characterized by low RH value and low T_d value, and the RH threshold for detecting SI events ranges from 30% to 50% (Ou-Yang et al., 2022). This indicates that the SI air masses reached Nanjing and significantly influenced the upper air over Nanjing. Figure 2b shows the temporal evolution of the vertical distribution of O_3 from ERA5 data for the period 7–12 May 2023 over Nanjing. It was found that there was a high O_3 values region at 600–850 hPa over Nanjing on the night of 7 May, then gradually down to near-surface over Nanjing (Figure 2b). During 7–12 May, the near-surface of Nanjing was affected by high concentrations of O_3 (Figure 2b), which is consistent with the results of dry-cold air affecting Nanjing based on radiosonde data (Figure 2a). It was well confirmed that the O_3-rich air masses from the SI process contributed to the high O_3 pollution over Nanjing, that is, the O_3 pollution in the YRD region on 7–12 May.

The wind at 850 hPa over Nanjing was weak on 8 May (00:00 LT–15:00 LT), with no strong vertical transport (Figure S6a in Supporting Information S1). Therefore, the O_3 could remain at 700–850 hPa over the period

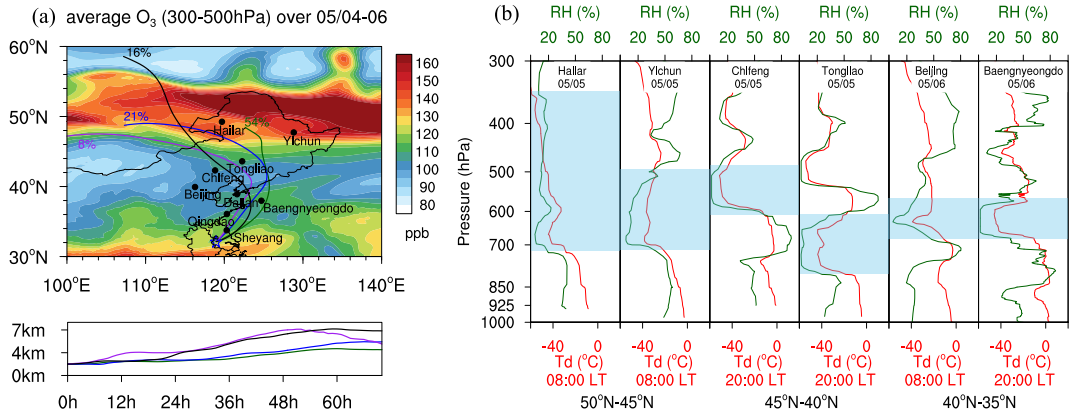

Figure 3. (a) 72-hr backward trajectories starting at an altitude of 1,500 m over Nanjing at 12:00 LT on 9 May 2023, filled with averaged O_3 at 300–500 hPa from 4 to 6 May 2023 based on ERA5 data. (b) Vertical RH and T_d profiles over Hailar (08:00 LT, 5 May), Yichun (08:00 LT, 5 May), Chifeng (20:00 LT, 5 May), Tongliao (20:00 LT, 5 May), Beijing (08:00 LT, 6 May), and Baengnyeongdo (20:00 LT, 6 May) based on radiosonde data.

(Figure 2b). Since the night of 8 May, the downwelling over Nanjing was enhanced (Figure S6b in Supporting Information S1), so the O_3 was able to be further transported downward (Figure 2b). While several enhancements of the downwelling happened in the following days, the O_3 was transported to the near-surface of Nanjing (Figures 2b and S6b in Supporting Information S1). The period corresponded with that of O_3 downward transporting (Figures 2b and S6b in Supporting Information S1).

3.2. Weather Process Analysis and Transport Pathway of SI O_3

The clustering analysis of 72-hr backward trajectories based on LPDM in Nanjing was performed to analyze the source of near-surface O_3 over Nanjing (Figure 3a). The 72-hr backward trajectories were started at an altitude of 1,500 m over Nanjing at 12:00 LT on 9 May. The clustering analysis of the backward trajectories reveals that the near-surface O_3 over Nanjing mainly comes from the high-altitude O_3 transport around 46°–60°N between 4 and 6 May, and there are high O_3 concentrations at 300–500 hPa at 46°–60°N (Figure 3a). The percentage of cluster 1 of the backward trajectories is 54%, which is from the regional high-altitude O_3 transport in the Inner Mongolia Autonomous Region and the northeast region of China (Figures 3a and S7a in Supporting Information S1). The percentage of cluster 2 from Mongolia's high-altitude O_3 transport is 21% (Figures 3a and S7b in Supporting Information S1). Cluster 3's percentage is 16%, which is from the high-altitude O_3 transport in southern Russia (Figures 3a and S7c in Supporting Information S1). The total percentage of clusters 1–3 is 92% while the percentage of cluster 4 is only 8% (Figures 3a and S7d in Supporting Information S1). Therefore, stratospheric invading O_3-rich air masses at 46°–60°N on 4–6 May (Figure 3a) reached Nanjing driven by high altitude wind fields (Figure S8 in Supporting Information S1), resulting in high O_3 pollution through regional transport processes.

Along the simulated air mass trajectories in Figure 3a, humidity measurement at six representative sounding sites as Hailar, Yichun, Chifeng, Tongliao, Beijing, and Baengnyeongdo (Figure 3a) were collected. Meanwhile, the latitude ranges are divided into three sections: 50°N–45°N, 45°N–40°N, and 40°N–35°N. Hailar and Yichun are located at 50°N–45°N, Chifeng and Tongliao are located at 45°N–40°N, while Beijing and Baengnyeongdo are located at 40°N–35°N. Since the four clusters start at different locations and the pathways of the four clusters are different, the heights of the dry-cold air in these selected six cities on the latitudinal band of the overall pathway do not follow a gradual decrease (Figure 3). Dry-cold air (characterized by low RH value and low T_d value) began to appear in Hailar and Yichun around 600–700 hPa at 08:00 LT on 5 May (Figure 3b). At 20:00 LT on 5 May, Chifeng was characterized by dry-cold air at approximately 500–600 hPa while Tongliao exhibited similar conditions at 650–750 hPa (Figure 3b). Next, dry-cold air appeared in Beijing at approximately 600 hPa at 08:00 LT on 6 May, then the dry-cold air passed over the Baengnyeongdo at approximately 600 hPa at 20:00 LT on the same day (Figure 3b). The stratospheric invading dry-cold air masses gradually passed over these six stations from 08:00 LT on 5 May (Figure 3b), eventually affecting Nanjing (Figure 2a). This is consistent with the

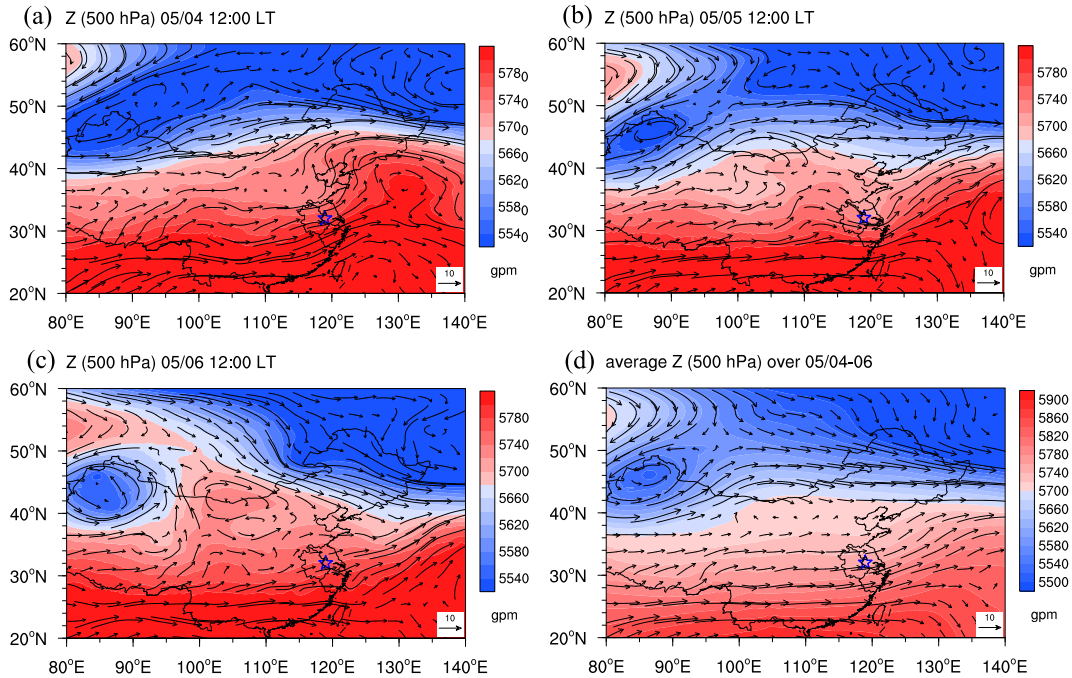

Figure 4. Spatial distribution of geopotential height (Z) at 500 hPa (a) at 12:00 LT on 4 May, (b) at 12:00 LT on 5 May, (c) at 12:00 LT on 6 May, and (d) averaged between 4 and 6 May based on ERA5 data. Vector arrows indicate the wind field at 500 hPa.

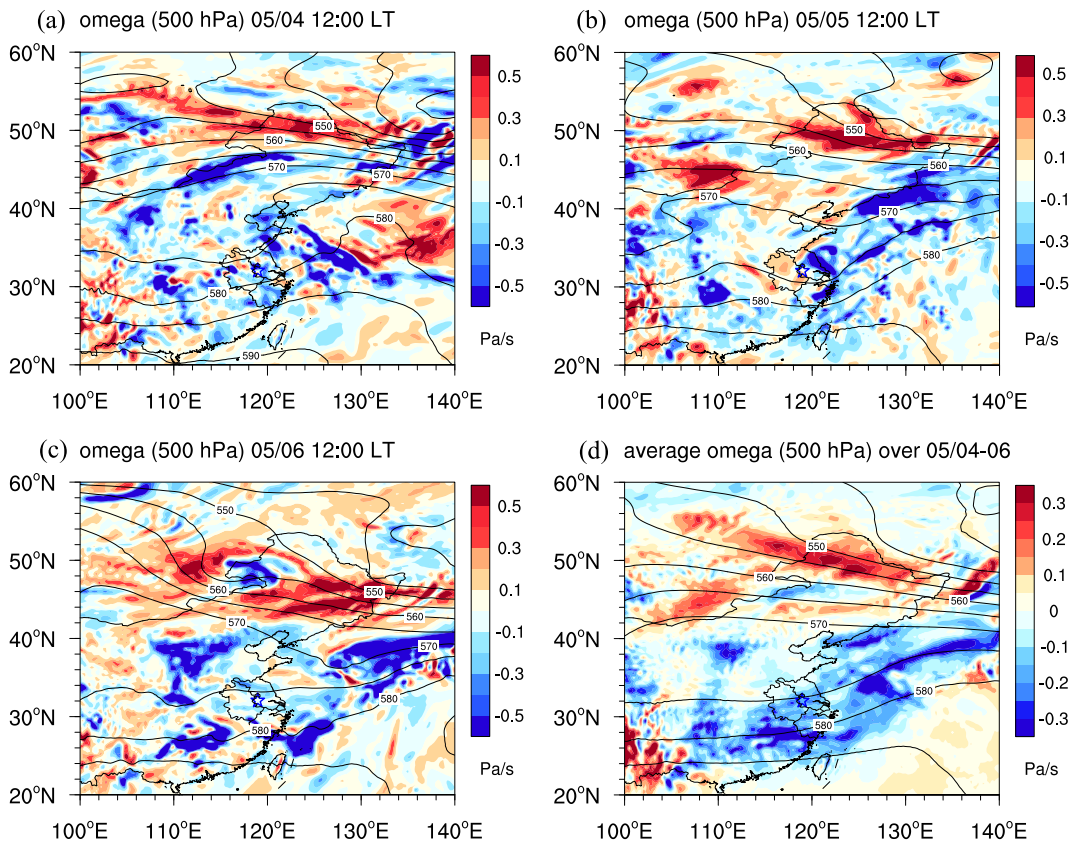

Figure 5. Spatial distribution of vertical velocity at 500 hPa (a) at 12:00 LT on 4 May, (b) at 12:00 LT on 5 May, (c) at 12:00 LT on 6 May, and (d) averaged on 4–6 May based on ERA5 data. The contours indicate the geopotential height at 500 hPa.

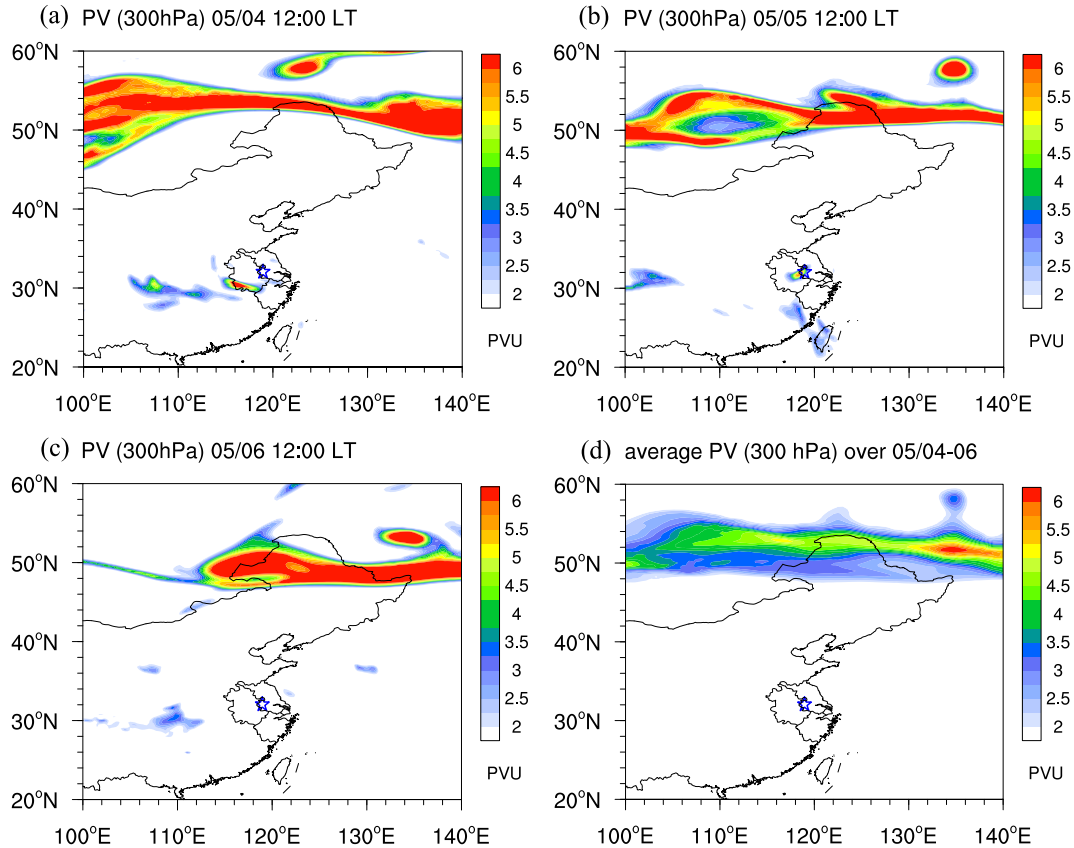

Figure 6. Spatial distribution of potential vorticity (PV) at 300 hPa (a) at 12:00 LT on 4 May, (b) at 12:00 LT on 5 May, (c) at 12:00 LT on 6 May, and (d) averaged on 4–6 May based on ERA5 data.

radiosonde profiles. This further confirms the transport of SI air masses with high levels of O_3 from northeastern China to the YRD region.

The above analysis highlights the effect of SI process on tropospheric O_3 variation. However, the underlying mechanisms of SI events remain unclear, and the extent to which SI contributes to near-surface O_3 over Nanjing remains unclear. To address this question, the weather process of the stratospheric intrusion of O_3 at 46°–60°N transported to Nanjing is analyzed. Figures 4a–4c show the spatial distribution of geopotential height (Z) at 500 hPa on 4–6 May. A low-pressure system was observed in the range of 80°–100°E and 40°–60°N, which was in the early developmental phase at 12:00 LT on 4 May (Figure 4a). Then the low-pressure system continued to develop, and was not fully enclosed at 12:00 LT on 5 May (Figure 4b). Up to 12:00 LT on 5 May, the wind field at 500 hPa was around the low-pressure system, which was persistent westerly winds near 40°N (Figures 4a and 4b). At 12:00 LT on 6 May, the closed low-pressure system was well developed and the wind field at 500 hPa had shifted to northwest winds (Figure 4c). Figure 4d shows the averaged spatial distribution of Z at 500 hPa between 4 and 6 May. After developing and maturing, the deep low-pressure system will gradually transport eastwards under the influence of winds (Figure 4d). In the process, the troughs that accompany the low-pressure system also moved eastwards. From 12:00 LT on 4 May to 12:00 LT on 6 May, the troughs gradually moved eastwards (Figures 4a–4c and 5a–5c). While the vertical velocity behind the troughs was positive, which indicates the strong downwelling (Figures 5a–5c). The strong downwelling was even more obvious from the averaged vertical velocity at 500 hPa in Figure 5d, which was all positive in the region the troughs moved. Consequently, accompanied by the downwelling behind the trough, the SI process occurs at 46°–60°N. Once the stratospheric O_3-rich dry-cold air masses inject the troposphere at 46°–60°N, they are driven by the high-altitude wind field, accompanied by strong downwelling, and gradually transported southward and downward according to the trajectories in Figures 3a and S4 in Supporting Information S1, ultimately affect the near-surface O_3 in the YRD region.

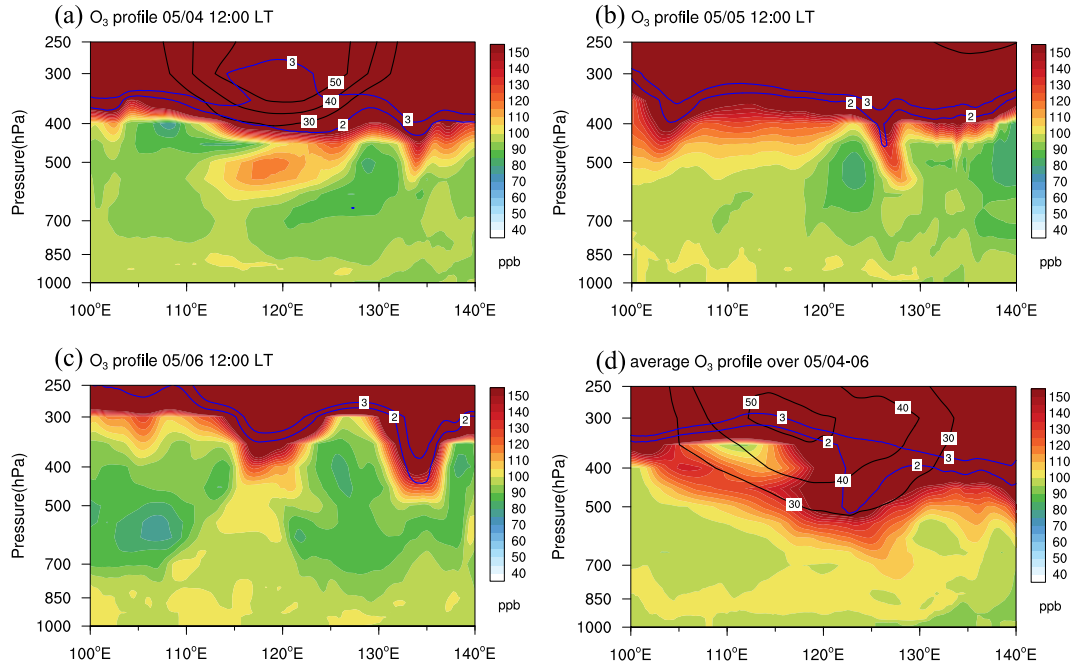

Figure 7. Longitude-height cross-section (averaged over 51°N–53°N) of O_3 (a) at 12:00 LT on 4 May, (b) at 12:00 LT on 5 May, (c) at 12:00 LT on 6 May, and (d) averaged on 4–6 May based on ERA5 data. Black lines indicate the zonal wind (U), and blue lines represent the PV values of 2PVU and 3PVU (1PVU = 10^{-6} K · m^2 · s^{-1} · kg^{-1}), respectively.

3.3. Quantitative Understanding on Regional Impacts of SI Ozone

SI processes can occur in the regions where strong downwelling occurs at high altitudes. The PV is a conserved quantity in the absence of heat sources and friction, which is widely used as a tracer to distinguish stratospheric and tropospheric airs. Following previous studies, 2 PVU (1PVU = 10^{-6} K · m^2 · s^{-1} · kg^{-1}) is commonly considered indicative of the dynamical tropopause (Wang, Wang, et al., 2020), which can well reflect the conservative feature of the atmosphere in adiabatic and frictionless circumstances. The rapid and irreversible deformation of PV often indicates the breaking of Rossby waves and the folding of the tropopause, which is associated with SI events. Figure 6 shows the spatial distribution of PV at 300 hPa on 4–6 May based on ERA5 data. Corresponding to the development of low-pressure systems (Figures 4a and 4b), the dynamical tropopause (2 PVU) is located at 80°–100°E and 40°–60°N on 4–5 May (Figures 6a and 6b), and is also located in the east (Figures 6a and 6b). Once low-pressure systems have matured, the dynamical tropopause (2 PVU) is located primarily east of 110°E (Figure 6c). Accompanied with these PV intrusions, stratospheric O_3-rich air masses were injected into the troposphere, and the intrusion area was banded based on the averaged PV on 4–6 May (Figure 6d). Figure 7 shows the longitude-height cross-section (averaged over 51°N–53°N) of O_3. It is found that high O_3 concentrations extend down to 400–500 hPa while the dynamical tropopause (2 PVU) reaches 400 hPa at 12:00 LT on 4 May (Figure 7a). This indicates a clear intrusion of stratospheric air from higher altitudes to lower altitudes in the troposphere. Zonal winds above 500 hPa are greater than 40 m/s, indicating the drive of high-altitude jets (Figure 7a), which resulting in the transport of stratospheric air into the troposphere (Figure 7a). At 12:00 LT on 5–6 May, despite the weakening of the high-altitude jets, the dynamical

Table 1
Statistical Quantity of 2 m Temperature (T2) and Ground Dew Point Temperature (T_d) in Nanjing From Observations (NCDC) and UBC Simulations

	Mean bias (Obs minus UBC)	IOA	RMSE	R^2
T2	1.56 K	0.92	2.34	0.84
T_d	3.08 K	0.62	3.65	0.48

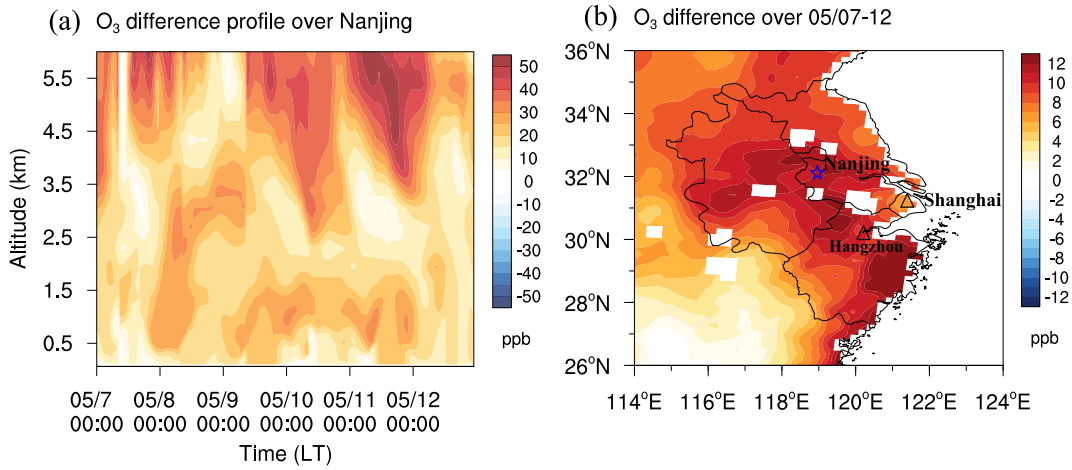

Figure 8. (a) Temporal evolution of the vertical distribution of O_3 difference over Nanjing, (b) spatial distribution of the averaged near-surface O_3 difference between UBC and NOUBC (UBC–NOUBC) on 7–12 May.

tropopause (2 PVU) at 400–500 hPa still indicates the occurrence of SI events (Figures 7b and 7c). At the same time stratospheric O_3 is transported into the troposphere at 500 hPa (Figures 7b and 7c). The averaged O_3 profile in Figure 7d shows stronger high-altitude jets, with the dynamical tropopause (2 PVU) extending up to 500 hPa, and high concentrations of O_3 being transported as far as 700 hPa during 5–6 May (Figure 7d). It suggested that there was a continuous transport of stratospheric O_3-rich air into the troposphere, driven by high-altitude jets.

The air masses injected into the troposphere were transported south-eastward, driven by the wind fields at high altitude (Figure 4), and eventually affected the YRD area (Figures 2 and 3). Since WRF-Chem without upper boundary conditions was unable to simulate the impact of stratospheric O_3 on the troposphere (Figure 1c), the WRF-chem simulation with the addition of upper boundary conditions (UBC) was designed to provide a better simulation of the effect of stratospheric O_3 on the YRD near-surface O_3. Figure S9 in Supporting Information S1 shows the spatial distribution of the maximum daily 8-hr average ozone (MDA8) near surface recorded by UBC simulation and air quality monitoring stations. It shows that the simulated MDA8 ozone on 7–12 May has high concentrations east of China, which is consistent with the observational MDA8 O_3 and has a high spatial positional correspondence (Figure S9 in Supporting Information S1). Meanwhile, the statistical variables show a good agreement between the UBC simulation and the NCDC data, which further suggests that our simulation data can be used (Table 1). Figure 8a shows the vertical distribution of O_3 difference (UBC−NOUBC) over Nanjing. It was found that there was a high O_3 difference area at an altitude of 0.5–3.5 km over Nanjing on the night of 7 May, then gradually down to near the surface of Nanjing (Figure 7a). During 7−12 May, the near surface of Nanjing has been affected by high O_3 concentration (Figure 7a), which is consistent with the result of ERA5 (Figure 2b). Figure 8b shows the averaged near-surface O_3 difference (UBC–NOUBC) over the YRD region during 7–12 May, which indicated that simulated the stratospheric O_3 affecting the near-surface of the YRD region more than 12 ppb (Figure 8b). The daily near-surface O_3 differences indicated that the near-surface O_3 in the YRD region increased by more than 14 ppb on 9 May, followed by lower O_3 increases in the next days, which lasted until 12 May (Figure S10 in Supporting Information S1). This consistent result is also evident in the nighttime O_3 recorded by air quality monitoring stations (Figure 1d).

4. Conclusions

In this study, combining meteorological reanalysis data, in situ observations, and a regional meteorology-chemistry coupled model were applied to analyze the severe O_3 pollution over the YRD region on 7–12 May 2023. Our findings reveal that the severe O_3 pollution cannot be solely attributed to photochemical processes, SI also contributes to the near-surface O_3 pollution. The clustering analysis of the backward trajectories shows that the O_3-rich air masses injected into the lower troposphere are primarily driven by westerly jets and downwelling behind the troughs accompanying the low-pressure weather system at 46°–60°N on 4–6 May 2023. The invading stratospheric O_3-rich air masses can be transported to the YRD region driven by the strong downwelling occurring

with a high-altitude wind field toward the south, eventually leading to the persistent and severe near-surface O_3 pollution events in the YRD region on 7–12 May 2023.

The regional meteorology-chemistry model WRF-Chem is employed to quantify the contribution of the SI process to near-surface O_3 in the YRD region. However, since only the tropospheric chemical processes are included, the model tends to underestimate the near-surface O_3 pollution over the YRD region. While coupling the real-time input of upper chemical boundary conditions, it is estimated that such regionally transported SI O_3 contributed more than 12 ppb to O_3 pollution over the YRD region. This study highlights the importance of future air quality models incorporating real-time stratospheric processes and the necessity to comprehensively understand atmospheric chemical and physical processes. Given that such SI events occur frequently over East Asia, it is of critical importance to investigate and quantify the natural processes (especially the SI events), in addition to anthropogenic emissions alone, in air quality forecasting and air pollution control in China.

Conflict of Interest

The authors declare no conflicts of interest relevant to this study.

Data Availability Statement

The WRF-Chem model is open-source air quality model from UCAR (https://www2.mmm.ucar.edu/wrf/users/). Meteorological input data for the WRF-Chem model were derived from NOAA public databases (https://rda.ucar.edu/datasets/). The national air quality monitoring data are archived at a repository of Chinese National Environmental Monitoring Center. The Wyoming radiosonde data set can be downloaded from the University of Wyoming (http://weather.uwyo.edu/upperair/sounding.html). Hourly observation of ground dew point temperature in May 2023 is provided by NOAA National Climatic Data Center (NCDC) (ftp://ftp.ncdc.noaa.gov/pub/data/noaa). The ERA5 reanalysis data were obtained from ECMWF (Hersbach et al., 2020). The WRF simulation data are archived on the Figshare platform at (Lu & Huang, 2024). All figures in this study are plotted by using NCAR Command Language (NCL), and related code can be found in NCL application examples (https://www.ncl.ucar.edu/Applications/).

Acknowledgments
This work was supported by the National Natural Science Foundation of China (42293322) and the National Key Research and Development Program of China (2023YFC3709401). We would like to acknowledge the global radiosonde observations are obtained from the University of Wyoming (UWYO), and acknowledge the European Centre for Medium-range Weather Forecasts (ECMWF) for providing the ERA5 products.

References

Akritidis, D., Zanis, P., Pytharoulis, I., Mavrakis, A., & Karacostas, T. (2010). A deep stratospheric intrusion event down to the earth's surface of the megacity of Athens. *Meteorology and Atmospheric Physics*, *109*(1–2), 9–18. https://doi.org/10.1007/s00703-010-0096-6

Ancellet, G., Beekmann, M., & Papayannis, A. (1994). Impact of a cutoff low development on downward transport of ozone in the troposphere. *Journal of Geophysical Research: Atmospheres*, *99*(D2), 3451–3468. https://doi.org/10.1029/93JD02551

Assareh, N., Prabamroong, T., Manomaiphiboon, K., Theramongkol, P., Leungsakul, S., Mitrjit, N., & Rachiwong, J. (2016). Analysis of observed surface ozone in the dry season over Eastern Thailand during 1997–2012. *Atmospheric Research*, *178*, 17–30. https://doi.org/10.1016/j.atmosres.2016.03.009

Bartusek, S., Wu, Y. T., Ting, M. F., Zheng, C., Fiore, A., Sprenger, M., & Flemming, J. (2023). Higher-resolution tropopause folding accounts for more stratospheric ozone intrusions. *Geophysical Research Letters*, *50*(8), e2022GL101690. https://doi.org/10.1029/2022GL101690

Chameides, W. L., Fehsenfeld, F., Rodgers, M. O., Cardelino, C., Martinez, J., Parrish, D., et al. (1992). Ozone precursor relationships in the ambient atmosphere. *Journal of Geophysical Research: Atmospheres*, *97*(D5), 6037–6055. https://doi.org/10.1029/91JD03014

Chen, D., Lü, D. R., & Chen, Z. Y. (2014). Simulation of the stratosphere-troposphere exchange process in a typical cold vortex over Northeast China. *Science China Earth Sciences*, *57*(7), 1452–1463. https://doi.org/10.1007/s11430-014-4864-x

Clifton, O. E., & Patton, E. G. (2021). Does organization in turbulence influence ozone removal by deciduous forests? *Journal of Geophysical Research-Biogeosciences*, *126*(6), 1–20. https://doi.org/10.1029/2021JG006362

Cooper, O. R. (2019). Detecting the fingerprints of observed climate change on surface ozone variability. *Science Bulletin*, *64*(6), 359–360. https://doi.org/10.1016/j.scib.2019.02.013

Ding, A. J., Fu, C. B., Yang, X. Q., Sun, J. N., Zheng, L. F., Xie, Y. N., et al. (2013). Ozone and fine particle in the western Yangtze River Delta: An overview of 1 yr data at the SORPES station. *Atmospheric Chemistry and Physics*, *13*(11), 5813–5830. https://doi.org/10.5194/acp-13-5813-2013

Ding, A. J., & Wang, T. (2006). Influence of stratosphere-to-troposphere exchange on the seasonal cycle of surface ozone at Mount Waliguan in western China. *Geophysical Research Letters*, *33*(3), L03803. https://doi.org/10.1029/2005GL024760

Ding, A. J., Wang, T., & Fu, C. B. (2013). Transport characteristics and origins of carbon monoxide and ozone in Hong Kong, South China. *Journal of Geophysical Research: Atmospheres*, *118*(16), 9475–9488. https://doi.org/10.1002/jgrd.50714

Ding, A. J., Wang, T., Thouret, V., Cammas, J. P., & Nédélec, P. (2008). Tropospheric ozone climatology over Beijing: Analysis of aircraft data from the MOZAIC program. *Atmospheric Chemistry and Physics*, *8*(1), 1–13. https://doi.org/10.5194/acp-8-1-2008

Ganguly, N. D., & Tzanis, C. (2011). Study of stratosphere-troposphere exchange events of ozone in India and Greece using ozonesonde ascents. *Meteorological Applications*, *18*(4), 467–474. https://doi.org/10.1002/met.241

Gaudel, A., Cooper, O. R., Ancellet, G., Barret, B., Boynard, A., Burrows, J. P., et al. (2018). Tropospheric Ozone Assessment Report: Present-day distribution and trends of tropospheric ozone relevant to climate and global atmospheric chemistry model evaluation. *Elementa-Science of the Anthropocene*, *6*, 39. https://doi.org/10.1525/elementa.291

Gerasopoulos, E., Zanis, P., Papastefanou, C., Zerefos, C. S., Ioannidou, A., & Wernli, H. (2006). A complex case study of down to the surface intrusions of persistent stratospheric air over the Eastern Mediterranean. *Atmospheric Environment*, *40*(22), 4113–4125. https://doi.org/10.1016/j.atmosenv.2006.03.022

Grell, G. A., Peckham, S. E., Schmitz, R., McKeen, S. A., Frost, G., Skamarock, W. C., & Eder, B. (2005). Fully coupled "online" chemistry within the WRF model. *Atmospheric Environment*, *39*(37), 6957–6975. https://doi.org/10.1016/j.atmosenv.2005.04.027

Gui, K., Che, H. Z., Chen, Q. L., Zeng, Z. L., Liu, H. Z., Wang, Y. Q., et al. (2017). Evaluation of radiosonde, MODIS-NIR-Clear, and AERONET precipitable water vapor using IGS ground-based GPS measurements over China. *Atmospheric Research*, *197*, 461–473. https://doi.org/10.1016/j.atmosres.2017.07.021

Hersbach, H., Bell, B., Berrisford, P., Hirahara, S., Horányi, A., Muñoz-Sabater, J., et al. (2020). The ERA5 global reanalysis. *Quarterly Journal of the Royal Meteorological Society*, *146*(730), 1999–2049. https://doi.org/10.1002/qj.3803

Holton, J. R., Haynes, P. H., Mcintyre, M. E., Douglass, A. R., Rood, R. B., & Pfister, L. (1995). Stratosphere-troposphere exchange. *Reviews of Geophysics*, *33*(4), 403–439. https://doi.org/10.1029/95RG02097

Hong, J., Wang, H. Y., Wang, W. K., Zhu, J. T., Deng, H. Y., & Wang, H. (2024). Impacts of stratosphere-to-troposphere transport on tropospheric ozone in southeastern China: Insights from ozonesonde observations. *Environmental Research Letters*, *19*(6), 064068. https://doi.org/10.1088/1748-9326/ad4ef9

Huang, X., Ding, A. J., Gao, J., Zheng, B., Zhou, D. R., Qi, X. M., et al. (2021). Enhanced secondary pollution offset reduction of primary emissions during COVID-19 lockdown in China. *National Science Review*, *8*(2). https://doi.org/10.1093/nsr/nwaa137

Huang, X., Wang, Z. L., & Ding, A. J. (2018). Impact of aerosol-PBL interaction on Haze pollution: Multiyear observational evidences in north China. *Geophysical Research Letters*, *45*(16), 8596–8603. https://doi.org/10.1029/2018GL079239

Huang, X., Zhou, L. X., Ding, A. J., Qi, X. M., Nie, W., Wang, M. H., et al. (2016). Comprehensive modelling study on observed new particle formation at the SORPES station in Nanjing, China. *Atmospheric Chemistry and Physics*, *16*(4), 2477–2492. https://doi.org/10.5194/acp-16-2477-2016

Krasauskas, L., Ungermann, J., Preusse, P., Friedl-Vallon, F., Zahn, A., Ziereis, H., et al. (2021). 3-D tomographic observations of Rossby wave breaking over the North Atlantic during the WISE aircraft campaign in 2017. *Atmospheric Chemistry and Physics*, *21*(13), 10249–10272. https://doi.org/10.5194/acp-21-10249-2021

Lamarque, J. F., Langford, A. O., & Proffitt, M. H. (1996). Cross-tropopause mixing of ozone through gravity wave breaking: Observation and modeling. *Journal of Geophysical Research: Atmospheres*, *101*(D17), 22969–22976. https://doi.org/10.1029/96JD02442

Langford, A. O., Alvarez, R. J., Brioude, J., Evan, S., Iraci, L. T., Kirgis, G., et al. (2018). Coordinated profiling of stratospheric intrusions and transported pollution by the Tropospheric Ozone Lidar Network (TOLNet) and NASA Alpha Jet Experiment (AJAX): Observations and comparison to HYSPLIT, RAQMS, and FLEXPART. *Atmospheric Environment*, *174*, 1–14. https://doi.org/10.1016/j.atmosenv.2017.11.031

Langford, A. O., Brioude, J., Cooper, O. R., Senff, C. J., Alvarez, R. J., Hardesty, R. M., et al. (2012). Stratospheric influence on surface ozone in the Los Angeles area during late spring and early summer of 2010. *Journal of Geophysical Research: Atmospheres*, *117*(D21). https://doi.org/10.1029/2011JD016766

Lefohn, A. S., Emery, C., Shadwick, D., Wernli, H., Jung, J., & Oltmans, S. J. (2014). Estimates of background surface ozone concentrations in the United States based on model-derived source apportionment. *Atmospheric Environment*, *84*, 275–288. https://doi.org/10.1016/j.atmosenv.2013.11.033

Lefohn, A. S., Malley, C. S., Smith, L., Wells, B., Hazucha, M., Simon, H., et al. (2018). Tropospheric ozone assessment report: Global ozone metrics for climate change, human health, and crop/ecosystem research. *Elementa-Science of the Anthropocene*, *6*, 39. https://doi.org/10.1525/elementa.279

Li, D., Bian, J. C., & Fan, Q. J. (2015). A deep stratospheric intrusion associated with an intense cut-off low event over East Asia. *Science China Earth Sciences*, *58*(1), 116–128. https://doi.org/10.1007/s11430-014-4977-2

Li, K., Jacob, D. J., Shen, L., Lu, X., De Smedt, I., & Liao, H. (2020). Increases in surface ozone pollution in China from 2013 to 2019: Anthropogenic and meteorological influences. *Atmospheric Chemistry and Physics*, *20*(19), 11423–11433. https://doi.org/10.5194/acp-20-11423-2020

Li, M. M., Huang, X., Yan, D., Lai, S. Y., Zhang, Z. H., Zhu, L., et al. (2024). Coping with the concurrent heatwaves and ozone extremes in China under a warming climate. *Science Bulletin*, *69*(18), 2938–2947. https://doi.org/10.1016/j.scib.2024.05.034

Li, Y. S., Yin, S. S., Yu, S. J., Bai, L., Wang, X. D., Lu, X., & Ma, S. L. (2021). Characteristics of ozone pollution and the sensitivity to precursors during early summer in central plain, China. *Journal of Environmental Sciences*, *99*, 354–368. https://doi.org/10.1016/j.jes.2020.06.021

Lin, M. Y., Fiore, A. M., Cooper, O. R., Horowitz, L. W., Langford, A. O., Levy, H., et al. (2012). Springtime high surface ozone events over the western United States: Quantifying the role of stratospheric intrusions. *Journal of Geophysical Research: Atmospheres*, *117*(D21). https://doi.org/10.1029/2012jd018151

Lin, W. L., Xu, X. B., Zheng, X. D., Dawa, J., Baima, C., & Ma, J. (2015). Two-year measurements of surface ozone at Dangxiong, a remote highland site in the Tibetan Plateau. *Journal of Environmental Sciences*, *31*, 133–145. https://doi.org/10.1016/j.jes.2014.10.022

Linsha, C. L., Reshma, T., Varikoden, H., & Vishnu, R. (2024). Thermodynamic and stability features of the atmospheric boundary layer over Kochi during different monsoon seasons based on radiosonde profiles. *Journal of Atmospheric and Solar-Terrestrial Physics*, *256*, 106209. https://doi.org/10.1016/j.jastp.2024.106209

Lu, J., & Huang, X. (2024). WRF simulation data during May 7 to 12, 2023 [Dataset]. *figshare*. https://doi.org/10.6084/m9.figshare.26816320.v1

Lu, X., Zhang, L., Chen, Y. F., Zhou, M., Zheng, B., Li, K., et al. (2019). Exploring 2016–2017 surface ozone pollution over China: Source contributions and meteorological influences. *Atmospheric Chemistry and Physics*, *19*(12), 8339–8361. https://doi.org/10.5194/acp-19-8339-2019

Lu, X., Zhang, L., Zhao, Y. H., Jacob, D. J., Hu, Y. Y., Hu, L., et al. (2019). Surface and tropospheric ozone trends in the southern Hemisphere since 1990: Possible linkages to poleward expansion of the Hadley circulation. *Science Bulletin*, *64*(6), 400–409. https://doi.org/10.1016/j.scib.2018.12.021

Monks, P. S., Archibald, A. T., Colette, A., Cooper, O., Coyle, M., Derwent, R., et al. (2015). Tropospheric ozone and its precursors from the urban to the global scale from air quality to short-lived climate forcer. *Atmospheric Chemistry and Physics*, *15*(15), 8889–8973. https://doi.org/10.5194/acp-15-8889-2015

Olsen, M. A., Manney, G. L., & Liu, J. H. (2019). The ENSO and QBO impact on ozone variability and stratosphere-troposphere exchange relative to the subtropical jets. *Journal of Geophysical Research: Atmospheres*, *124*(13), 7379–7392. https://doi.org/10.1029/2019jd030435

Ou-Yang, C. F., Babu, S. R., Lee, J. R., Yen, M. C., Griffith, S. M., Lin, C. C., et al. (2022). Detection of stratospheric intrusion events and their role in ozone enhancement at a mountain background site in sub-tropical East Asia. *Atmospheric Environment*, *268*, 118779. https://doi.org/10.1016/j.atmosenv.2021.118779

Poulida, O., Dickerson, R. R., & Heymsfield, A. (1996). Stratosphere-troposphere exchange in a midlatitude mesoscale convective complex. *Journal of Geophysical Research: Atmospheres*, *101*(D3), 6823–6836. https://doi.org/10.1029/95JD03523

Price, J. D., & Vaughan, G. (1993). The potential for stratosphere troposphere exchange in cut-off-low systems. *Quarterly Journal of the Royal Meteorological Society*, *119*(510), 343–365. https://doi.org/10.1002/qj.49711951007

Salby, M. L., & Callaghan, P. F. (2006). Influence of the Brewer-Dobson circulation on stratosphere-troposphere exchange. *Journal of Geophysical Research: Atmospheres*, *111*(D21). https://doi.org/10.1029/2006JD007051

Sillman, S. (1995). The Use of NOy, H_2O_2, and HNO_3 as indicators for ozone-NOx-hydrocarbon sensitivity in urban locations. *Journal of Geophysical Research: Atmospheres*, *100*(D7), 14175–14188. https://doi.org/10.1029/94JD02953

Stein, A. F., Draxler, R. R., Rolph, G. D., Stunder, B. J. B., Cohen, M. D., & Ngan, F. (2015). NOAA's Hysplit atmospheric transport and dispersion modeling system. *Bulletin of the American Meteorological Society*, *96*(12), 2059–2077. https://doi.org/10.1175/Bams-D-14-00110.1

Stevenson, D. S., Dentener, F. J., Schultz, M. G., Ellingsen, K., van Noije, T. P. C., Wild, O., et al. (2006). Multimodel ensemble simulations of present-day and near-future tropospheric ozone. *Journal of Geophysical Research: Atmospheres*, *111*(D8), D08301. https://doi.org/10.1029/2005JD006338

Stohl, A., Bonasoni, P., Cristofanelli, P., Collins, W., Feichter, J., Frank, A., et al. (2003). Stratosphere-troposphere exchange:: A review, and what we have learned from STACCATO -: Art. No. 8516. *Journal of Geophysical Research: Atmospheres*, *108*(D12). https://doi.org/10.1029/2002JD002490

Sun, Y. L., Yang, F., Liu, M. J., Li, Z. C., Gong, X., & Wang, Y. Y. (2023). Evaluation of the weighted mean temperature over China using multiple reanalysis data and radiosonde. *Atmospheric Research*, *285*, 106664. https://doi.org/10.1016/j.atmosres.2023.106664

Tang, G., Wang, Y., Li, X., Ji, D., Hsu, S., & Gao, X. (2012). Spatial-temporal variations in surface ozone in Northern China as observed during 2009–2010 and possible implications for future air quality control strategies. *Atmospheric Chemistry and Physics*, *12*(5), 2757–2776. https://doi.org/10.5194/acp-12-2757-2012

Tarasick, D. W., Carey-Smith, T. K., Hocking, W. K., Moeini, O., He, H., Liu, J., et al. (2019). Quantifying stratosphere-troposphere transport of ozone using balloon-borne ozonesondes, radar wind profilers and trajectory models. *Atmospheric Environment*, *198*, 496–509. https://doi.org/10.1016/j.atmosenv.2018.10.040

Wang, H. Y., Wang, W., Huang, X., & Ding, A. J. (2020). Impacts of stratosphere-to-troposphere-transport on summertime surface ozone over eastern China. *Science Bulletin*, *65*(4), 276–279. https://doi.org/10.1016/j.scib.2019.11.017

Wang, H. Y., Wang, W. K., Shangguan, M., Wang, T. Y., Hong, J., Zhao, S. Y., & Zhu, J. T. (2023). The stratosphere-to-troposphere transport related to Rossby wave breaking and its impact on summertime ground-level ozone in eastern China. *Remote Sensing*, *15*(10), 2647. https://doi.org/10.3390/rs15102647

Wang, N., Wang, H. Y., Huang, X., Chen, X., Zou, Y., Deng, T., et al. (2024). Extreme weather exacerbates ozone pollution in the Pearl River Delta, China: Role of natural processes. *Atmospheric Chemistry and Physics*, *24*(2), 1559–1570. https://doi.org/10.5194/acp-24-1559-2024

Wang, T., Xue, L. K., Brimblecombe, P., Lam, Y. F., Li, L., & Zhang, L. (2017). Ozone pollution in China: A review of concentrations, meteorological influences, chemical precursors, and effects. *Science of the Total Environment*, *575*, 1582–1596. https://doi.org/10.1016/j.scitotenv.2016.10.081

Wang, Z. L., Huang, X., Wang, N., Xu, J. W., & Ding, A. J. (2020). Aerosol-radiation interactions of dust storm deteriorate particle and ozone pollution in East China. *Journal of Geophysical Research-Atmospheres*, *125*(24), e2020JD033601. https://doi.org/10.1029/2020jd033601

Xia, Y., Hu, Y. Y., Huang, Y., Bian, J. C., Zhao, C. F., Wei, J., et al. (2022). Concurrent hot extremes and high ultraviolet radiation in summer over the Yangtze Plain and their possible impact on surface ozone. *Environmental Research Letters*, *17*(6), 064001. https://doi.org/10.1088/1748-9326/ac6c3c

Xia, Y., Xie, F., & Lu, X. (2023). Enhancement of Arctic surface ozone during the 2020–2021 winter associated with the sudden stratospheric warming. *Environmental Research Letters*, *18*(2), 024003. https://doi.org/10.1088/1748-9326/acaee0

Xu, J. W., Huang, X., Wang, N., Li, Y. Y., & Ding, A. J. (2021). Understanding ozone pollution in the Yangtze River Delta of eastern China from the perspective of diurnal cycles. *Science of the Total Environment*, *752*, 141928. https://doi.org/10.1016/j.scitotenv.2020.141928

Xu, X., Lin, W., Wang, T., Yan, P., Tang, J., Meng, Z., & Wang, Y. (2008). Long-term trend of surface ozone at a regional background station in eastern China 1991–2006: Enhanced variability. *Atmospheric Chemistry and Physics*, *8*(10), 2595–2607. https://doi.org/10.5194/acp-8-2595-2008

Xue, L., Ding, A. J., Cooper, O., Huang, X., Wang, W. K., Zhou, D. R., et al. (2021). ENSO and Southeast Asian biomass burning modulate subtropical trans-Pacific ozone transport. *National Science Review*, *8*(6). https://doi.org/10.1093/nsr/nwaa132

Yang, Y., Wang, Z. L., Lou, S. J., Xue, L., Lu, J. P., Wang, H. Y., et al. (2022). Strong ozone intrusions associated with super dust storms in East Asia. *Atmospheric Environment*, *290*, 119355. https://doi.org/10.1016/j.atmosenv.2022.119355

Young, P. J., Naik, V., Fiore, A. M., Gaudel, A., Guo, J., Lin, M. Y., et al. (2018). Tropospheric ozone assessment report: Assessment of global-scale model performance for global and regional ozone distributions, variability, and trends. *Elementa-Science of the Anthropocene*, *6*. https://doi.org/10.1525/ELEMENTA.265/112813

Zhang, Y. J., Li, J., Yang, W. Y., Du, H. Y., Tang, X., Ye, Q., et al. (2022). Influences of stratospheric intrusions to high summer surface ozone over a heavily industrialized region in northern China. *Environmental Research Letters*, *17*(9), 094023. https://doi.org/10.1088/1748-9326/ac8b24

Zhao, P., Zhou, X. J., Chen, J. M., Liu, G., & Nan, S. L. (2019). Global climate effects of summer Tibetan Plateau. *Science Bulletin*, *64*(1), 1–3. https://doi.org/10.1016/j.scib.2018.11.019